

Unravelling the effects of active site density and energetics on the water oxidation activity of iridium oxides

Received: 19 February 2023

Accepted: 23 April 2024

Published online: 7 June 2024

Check for updates

Caiwu Liang^{1,2}, Reshma R. Rao^{1,2}✉, Katrine L. Svane³, Joseph H. L. Hadden¹, Benjamin Moss², Soren B. Scott¹, Michael Sachs⁴, James Murawski¹, Adrian Malthe Frandsen³, D. Jason Riley¹, Mary P. Ryan¹, Jan Rossmeisl³✉, James R. Durrant²✉ & Ifan E. L. Stephens¹✉

Understanding what controls the reaction rate on iridium-based catalysts is central to designing better electrocatalysts for the water oxidation reaction in proton exchange membrane electrolyzers. Here we quantify the densities of redox-active centres and probe their binding strengths on amorphous IrO_x and rutile IrO₂ using operando time-resolved optical spectroscopy. We establish a quantitative experimental correlation between the intrinsic reaction rate and the active-state energetics. We find that adsorbed oxygen species, *O, formed at water oxidation potentials, exhibit repulsive adsorbate–adsorbate interactions. Increasing their coverage weakens their binding, thereby promoting O–O bond formation, which is the rate-determining step. These analyses suggest that although amorphous IrO_x exhibits a higher geometric current density, the intrinsic reaction rates per active state on IrO_x and IrO₂ are comparable at given potentials. Finally, we present a modified volcano plot that elucidates how the intrinsic water oxidation kinetics can be increased by optimizing both the binding energy and the interaction strength between the catalytically active states.

Water electrolysis via proton exchange membrane electrolyzers is a key technology for converting renewable energy into green hydrogen^{1,2}. However, the highly acidic and oxidizing conditions at the anode have thus far limited the choice of catalysts for the kinetically sluggish water oxidation reaction to oxides of iridium³. Iridium is one of the scarcest elements on the planet, with a production potential of <9 t yr⁻¹ (ref. 4). Consequently, one of the key challenges for the terawatt-scale uptake of proton exchange membrane electrolyzers is to minimise the iridium loading at the anode^{4–8}.

A number of iridium-based oxides have been studied, ranging from crystalline rutile oxides, amorphous oxides and alloyed oxides^{9–12} to perovskites^{13,14}. The catalytic activity is usually compared by

normalizing the current density to the geometric area or the mass of iridium. Amorphous IrO_x is more active but less stable than crystalline rutile IrO₂, and shows a 220 mV reduction in overpotential as well as an approximately two orders of magnitude lower lifetime at 1 mA cm⁻²_{geo} (ref. 8). Recent studies on highly active IrNiO_x (refs. 10,11), Li–IrO_x (ref. 9) and SrIrO_x (refs. 8,13,15) have demonstrated that the surface of these materials is converted to an amorphous phase on exposure to oxygen evolution reaction (OER) potentials. Amorphous IrO_x is easier to oxidize and undergoes greater Ir–O bond shortening with increased potential compared with crystalline IrO₂ (refs. 9,10,16,17). These differences in coordination environment of the iridium centre have been suggested to influence the binding energetics of key OER intermediates, possibly

¹Department of Materials, Imperial College London, London, UK. ²Department of Chemistry, Centre for Processable Electronics, Imperial College London, London, UK. ³Department of Chemistry, University of Copenhagen, Copenhagen, Denmark. ⁴PULSE Institute, Stanford University, Menlo Park, CA, USA.

✉e-mail: reshma.rao@imperial.ac.uk; jan.rossmeisl@chem.ku.dk; j.durrant@imperial.ac.uk; i.stephens@imperial.ac.uk

resulting in the differences in activity observed^{11,16,18–21}. However, the detailed mechanistic origins of the differences in activity between amorphous IrO_x and rutile IrO₂ remain poorly understood.

Studies as far back as the 1950s have suggested that water oxidation on metal oxides can proceed via sequential steps of proton-coupled electron transfer to form an O₂ molecule^{22,23}. More recently, density functional theory (DFT) models have suggested that the potential-determining step for the OER on iridium oxide is the reaction of adsorbed oxygen (*O) with water to form a peroxo intermediate (*OOH): *O + H₂O → *OOH + H⁺ + e⁻ (that is, O–O bond formation), where e⁻ is an electron^{24,25}. Recent work by Nong et al., combining X-ray absorption spectroscopy (XAS) and DFT, has also implied that this step is the rate-determining step (RDS)²⁶. Crucially however, Nong and co-workers suggest that the activation energy of the RDS decreases linearly with *O coverage, attributed to long-range interactions between *O species. Our recent work using operando optical spectroscopy agrees with this conclusion: an increase in OER kinetics correlates with the density of accumulated oxidized species (*O) on amorphous IrO_x. Conversely, using an immobilized molecular iridium catalyst, where these cooperative interactions are absent, the water oxidation kinetics were independent of *O coverage^{27–29}. Although the importance of adsorbate–adsorbate interactions has been raised by Nong et al., it remains unclear how adsorbate–adsorbate interactions influence the trend in activity from one catalyst to another. This lack of quantitative understanding is derived from the difficulties in theoretically and experimentally determining electroadsorption isotherms and turnover frequencies on catalysts, with the exception of single crystals³⁰.

Here we use operando optical spectroscopy to compare the water oxidation energetics and kinetics of amorphous IrO_x versus crystalline rutile IrO₂. We quantitatively determine the density of redox-active centres as a function of the potential and quantify the interaction between adsorbate species by experimentally determining the electroadsorption isotherms for both amorphous IrO_x and rutile IrO₂. The location of redox-active centres is spatially resolved using isotope labelling and time-of-flight secondary-ion mass spectrometry (ToF-SIMS). The structure and local environment of the catalysts is probed using XAS. Finally, time-resolved optical spectroscopy is used to determine the intrinsic turnover frequency (TOF) values as a function of the potential. These results are corroborated with DFT calculations. By experimentally probing the potential-dependent density of active states, adsorbate–adsorbate interactions and TOF data, this study elucidates the key roles played by the electronic structure of the active site in governing the binding energy at zero coverage, in addition to the adsorbate–adsorbate interactions in controlling the weakening of the binding energy with increasing coverage, both of which control the kinetics of water oxidation. Taken together these effects reveal mechanistic origins of the differences in activity between amorphous IrO_x and rutile IrO₂ for water oxidation and provide rational design strategies for the discovery of water oxidation catalysts.

Results

Iridium local structure and its influence on proton penetration

In this study, hydrous, amorphous iridium oxide films (IrO_x, possibly hydroxylated in the as-prepared form) were prepared via electro-deposition on fluorine-doped tin oxide (FTO) glass substrates using a well-established procedure^{27,31} (see Methods for synthesis). Rutile IrO₂ films were obtained via thermal annealing of the electrodeposited IrO_x films at 550 °C for 8 h, as confirmed via X-ray diffraction (see Supplementary Note 1 and Supplementary Fig. 1c for details). Scanning electron microscopy (SEM) images show that amorphous films consist of nanoparticles 100–200 nm in size, whereas rutile IrO₂ has a larger particle size due to the growth of crystals during annealing (Supplementary Fig. 1a,b). However, in the as-deposited state, IrO_x shows a combination of Ir³⁺ and Ir⁴⁺ redox states, whereas IrO₂ is dominated by Ir⁴⁺, as determined using X-ray photoelectron spectroscopy

(XPS) (Supplementary Fig. 1d), consistent with previous work^{19,32}. This is further supported by ex situ XANES (X-ray absorption near-edge structure) measurements at the iridium L₃ edge. The average oxidation state is determined by the position of the white line edge, which primarily corresponds to a transition from occupied 2*p* to empty 5*d* states¹⁰. As shown in Supplementary Fig. 2, the *d*-band holes for amorphous IrO_x and rutile IrO₂ are at -4.4 and 5.0, corresponding to average oxidation states of around 3.4 and 4.0, respectively (see Methods for XANES measurements and analysis). The fitted EXAFS (extended X-ray absorption fine structure) results (Fig. 1c, Supplementary Fig. 3 and Supplementary Table 1) show that both samples have a characteristic Ir–O interatomic distance of ~2.0 Å, with comparable first-shell coordination numbers of 5.8 (±0.5) and 6.0 (±0.7) for amorphous IrO_x and rutile IrO₂, respectively. However, rutile IrO₂ shows a stronger signal from Ir–Ir₁ and Ir–Ir₂ (an interatomic distance between 2.5 and 4 Å) whereas these signals are very weak in amorphous IrO_x. Thus, these data suggest that short-range ordered [IrO₆] units are dominant for amorphous IrO_x whereas a longer-range ordered structure is present in rutile IrO₂, as shown schematically in Fig. 1a,b.

Compared with IrO₂, the cyclic voltammograms of IrO_x show higher redox current densities of around one order of magnitude, when normalized to the geometric area. IrO_x also shows a higher activity than IrO₂, as reflected in the overpotential required to achieve 0.5 mA cm⁻²_{geo} (~210 mV and 330 mV for IrO_x and IrO₂, respectively; Fig. 1d). IrO_x shows two distinct broad redox peaks at around 0.8 and 1.2 V versus the reversible hydrogen electrode (RHE). By contrast, no distinct redox peak can be observed for IrO₂. The redox features and catalytic activity of both samples are relatively stable for 20 cycles and 2.5 h of operation (further results on the stability of the redox features, activity and morphology/structure can be found in Supplementary Note 2).

To determine whether the increased current density on amorphous IrO_x is only a consequence of a higher permeability of electrolyte within the porous structure (resulting in a higher density of catalytically active sites) or is also a result of higher proton penetration through the bulk of the oxide (resulting in the participation of subsurface iridium sites), a combination of ToF-SIMS and deuterium isotope labelling was used. The film was impregnated and covered with paraffin wax, using an adapted method from Hadden and colleagues³³. This method minimizes the effects of varying porosity on the ion incorporation (see Fig. 1e and Supplementary Note 3 for details)—and thus focuses on the effect of surface exchange and bulk participation. However, we acknowledge that it may not completely eliminate the effects of extremely small pores within this hydrous oxide. Samples were cycled in 0.1 M DClO₄ (99.8% D) from 0.66 to 1.50 V_{RHE}. The depth of proton penetration during water oxidation was assessed by comparing the deuterium signal intensity between the cycled samples and those exposed only to the electrolyte but without electrochemical cycling. Figure 1f shows that amorphous IrO_x cycled in DClO₄ has a higher D/H ratio than the sample without cycling, for the first 100 s of ion sputtering, corresponding to a distance of around 20 nm. This signal then drops to the same level after 100 s (see Supplementary Figs. 7–10 and Supplementary Table 2 for details). By contrast, no obvious difference in D/H ratio can be observed before and after cycling for rutile IrO₂. These results indicate that protons penetrate far deeper into amorphous IrO_x than rutile IrO₂ under rounds of cyclic voltammetry (CV), thus offering more iridium sites for redox reactions and possibly for water oxidation. We conjecture that the short-range ordered structure in amorphous IrO_x is more flexible and hence allows more protons to access than the long-range ordered—and hence presumably more rigid—structure in rutile IrO₂. This is also consistent with the observation from atom probe tomography, by Mayrhofer, Cherevko, Gault, Kasian and co-workers^{34,35}, which indicates that hydrous IrO_x undergoes a greater degree of oxygen exchange with the electrolyte during OER than rutile IrO₂ where exchange is limited to within 2.5 nm of the surface.

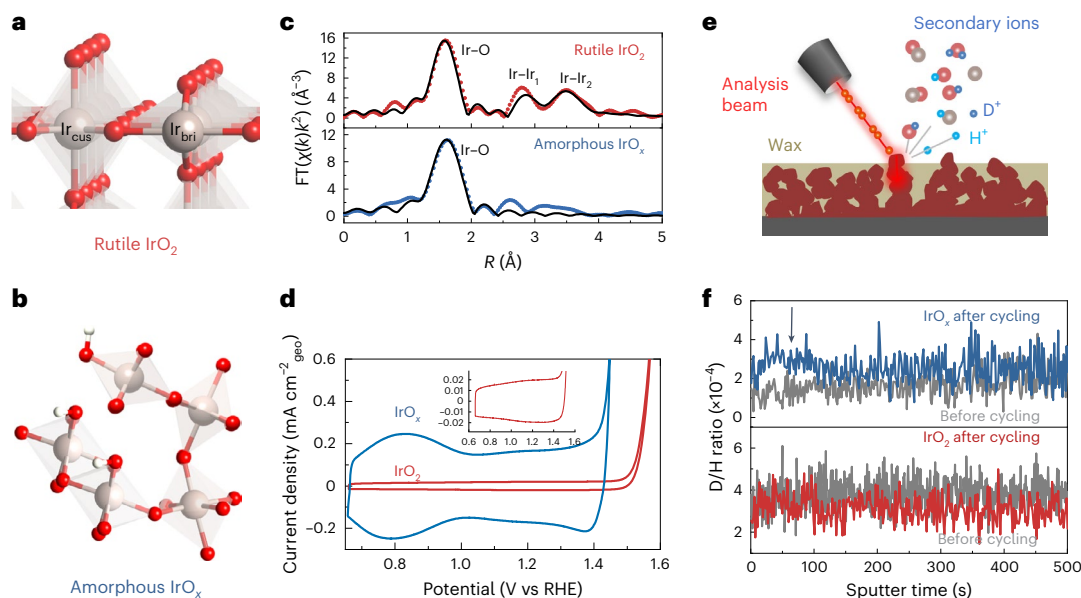


Fig. 1 Structure, composition and electrochemical behaviour of amorphous IrO_x and rutile IrO_2 . **a, b**, Possible crystal structures of rutile IrO_2 (**a**) and amorphous IrO_x (**b**). Grey, red and white spheres represent iridium, oxygen and hydrogen atoms, respectively. Ir_{cus} denotes a coordinatively unsaturated iridium site and Ir_{bri} denotes an iridium site bound to the bridging oxygen. **c**, Ex situ k^2 -weighted Fourier transform (FT) of EXAFS spectra collected at the iridium L_3 edge of amorphous IrO_x and rutile IrO_2 , showing the iridium coordination environment. Experimental data (solid lines) and fits (dotted lines) are shown. R , interatomic distance. **d**, Cyclic voltammograms of amorphous IrO_x and rutile IrO_2 with the same iridium loading obtained at a scan rate of 10 mV s^{-1} in 0.1 M

HClO_4 electrolyte (curves are iR -corrected (i , current; R , resistance)). Cyclic voltammograms are obtained after five cycles. The inset shows an expansion of the cyclic voltammogram of rutile IrO_2 . **e**, Schematic showing procedures for using ToF-SIMS to detect proton penetration in iridium oxides. Dark red polygons denote iridium oxides and the dark yellow rectangle represents the wax-covered surface. Light blue and dark blue spheres denote protons (H^+) and deuterium ions (D^+), respectively. **f**, Comparison of the D/H ratio change with ToF-SIMS sputter time in amorphous IrO_x and rutile IrO_2 before and after electrochemical cycling in deuterated HClO_4 solution. The downward arrow points to the region where a higher deuterium signal was observed compared to the background.

Identification of redox transitions on IrO_x and IrO_2

Next, we probe the redox chemistry of both materials using time-resolved operando ultraviolet-visible (UV–visible) spectroscopy and stepped potential spectroelectrochemistry (see Supplementary Note 4 for details). Figure 2a,b shows the change in the UV–visible absorption spectra (versus $0.66 \text{ V}_{\text{RHE}}$) when the potential is increased in 20 mV steps, reflecting the change in the surface speciation of the iridium oxides as a function of the potential. On increasing the potential, amorphous IrO_x shows broad absorption bands at 600 , 800 and 500 nm in the potential ranges of -0.66 – $1.00 \text{ V}_{\text{RHE}}$, -1.10 – $1.32 \text{ V}_{\text{RHE}}$ and $>1.32 \text{ V}_{\text{RHE}}$, respectively (Fig. 2a). We note that these absorption spectra are highly reversible with the potential and are reproducible over several cycles, showing almost identical absorption spectra during both the forward and reverse scans. (Supplementary Figs. 12 and 13). The absorption spectra of IrO_2 show an increasing pattern similar to IrO_x , with a slight shift of the dominant absorption band to higher wavelength in the low potential regime (Fig. 2b). However, the intensity of the optical absorption is around six times lower in the case of IrO_2 , consistent with this more crystalline and rigid structure having a lower density of redox-active iridium centres, as discussed above.

In optical spectroscopy, a change in absorbance between two potentials indicates a redox transition from one state to another. For each transition, we expect a distinct spectral shape for the change in absorbance^{27,28,36–38}. To discern these transitions, we analyse the change in absorbance at each potential by subtracting the spectra at adjacent potentials in intervals of 20 mV and normalize these differences to their maximum values. This process defines our differential spectra, as shown in Fig. 2c. We note that all differential spectra are positive in the measured wavelength window, which is a result of a continuous increase in absorption with the increasing applied potential (Fig. 2a). This differs from typical molecular systems, which often display isosbestic points in absorption and thus both positive and

negative regions in their differential spectra. However, this behaviour is not unique to our study and has been similarly observed in various metal oxide OER catalysts^{37–39}. This is most likely because the widths of the observed spectral features are greater than the measured spectral range. From Fig. 2c, three distinct differential absorption spectral features can be obtained: a converging spectral shape with a peak at $\sim 600 \text{ nm}$ between 0.66 and $0.90 \text{ V}_{\text{RHE}}$, a peak at $\sim 800 \text{ nm}$ between 1.1 and $1.3 \text{ V}_{\text{RHE}}$, and a peak at $\sim 500 \text{ nm}$ at potentials $>1.4 \text{ V}_{\text{RHE}}$. In other potential regions, a continuously changing spectral shape was observed, implying a combination of more than one redox transition process occurring. These constant differential spectra (as shown in Fig. 2d) correspond to the change in absorbance from one redox state to another (that is, $\text{state}_A \rightarrow \text{state}_B$, $\text{state}_B \rightarrow \text{state}_C$ and $\text{state}_C \rightarrow \text{state}_D$), and thus are denoted, respectively, as redox transition 1, redox transition 2 and redox transition 3, in accordance with our previous work (see Supplementary Note 5 for a detailed discussion)^{27,28}. Three distinct spectral components are also observed for IrO_2 , analogous to the three redox transitions observed for IrO_x (see the detailed discussion in Supplementary Note 5 and Supplementary Fig. 14), with similar (but anodically shifted, see below) potential dependencies. For IrO_2 , the peak position of redox transition 1 is shifted to 700 nm , and thus exhibits greater spectral overlap with redox transition 2; however, our deconvolution analyses clearly indicate that these two components can still be clearly resolved and their potential dependencies determined (Supplementary Figs. 16–18). These results show that, although IrO_x and IrO_2 have substantially different CVs, they undergo the same redox transition processes, with both generating three similar redox transitions in the applied potential range. This is in agreement with a recent study that observed comparable changes in iridium $4f$ XPS spectra and oxygen K -edge XAS spectra with potential on both amorphous IrO_x and crystalline IrO_2 (ref. 40).

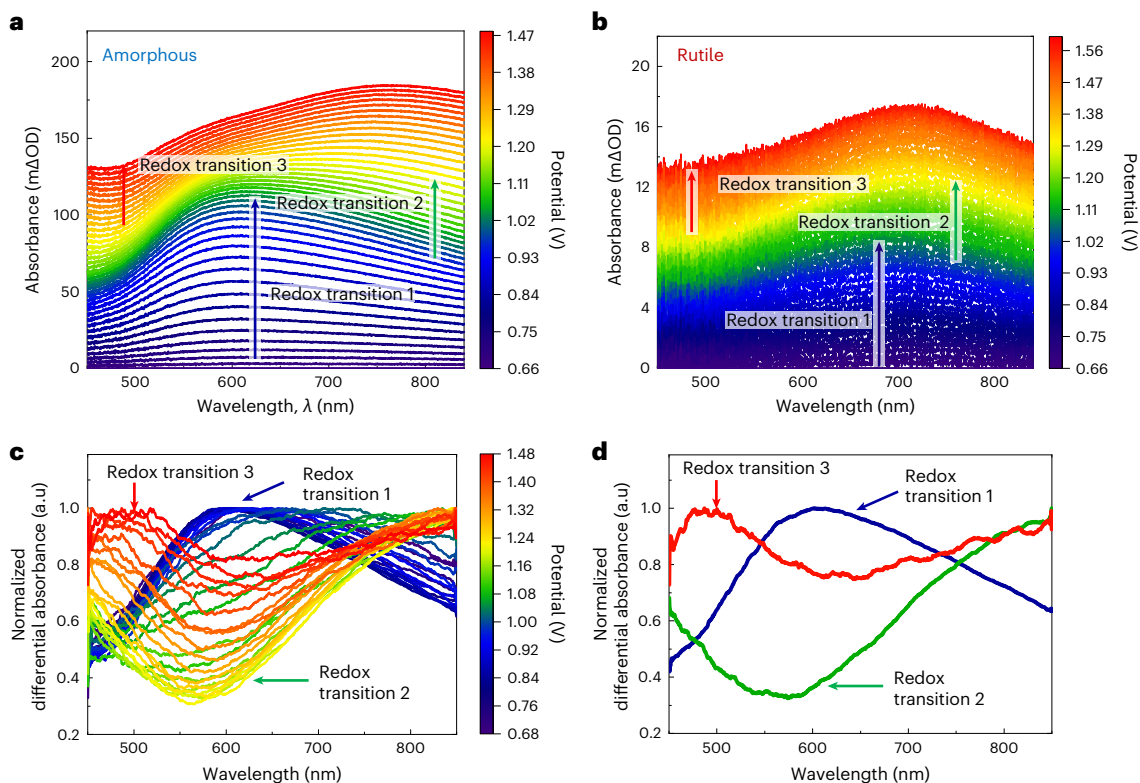


Fig. 2 | Redox transition features as function of the potential in amorphous IrO_x and rutile IrO_2 . **a**, Differential absorption spectra of amorphous IrO_x during a linear sweep scan from 0.66 to 1.48 V_{RHE} in 0.1 M HClO_4 at a scan rate of 1 mV s^{-1} (*iR*-corrected). Absorbance changes were recorded after five CV cycles, at every 1 mV (see Supplementary Fig. 11 for the full spectra) and shown every 20 mV. The changes in absorbance are calculated with respect to the absorbance at 0.66 V_{RHE} . **b**, Differential absorption spectra of rutile IrO_2 during a linear sweep scan from 0.66 to 1.60 V_{RHE} in 0.1 M HClO_4 at a scan rate of 1 mV s^{-1} (*iR*-corrected). **c**, Differential analysis of absorption spectra for amorphous IrO_x at every 20 mV.

The differential absorption spectra are obtained by subtracting adjacent spectra and normalizing the maximum absorbance to unity, representing a change in absorbance that corresponds to a potential change of 20 mV. **d**, Extracted spectra for individual redox transitions in amorphous IrO_x . The absorption spectra for redox transition 1 (blue), 2 (green) and 3 (red) in amorphous IrO_x are extracted from the potential regime where the shapes of the spectra in **c** are invariant, corresponding to differential spectra between 0.84 and 0.82 V_{RHE} , 1.18 and 1.16 V_{RHE} , and 1.46 and 1.44 V_{RHE} , respectively.

Quantification of redox transitions on IrO_x and IrO_2

To analyse the contribution of each redox transition to the observed spectra as function of the potential, we deconvoluted the absorption spectra through a linear combination fitting process. Specifically, we fitted the measured absorption spectra at each potential to a linear sum of the component spectra corresponding to different redox transitions. The fitting process, applied individually to the spectra at each potential, does not require assumptions about the potential dependence of various redox-state densities. It solely requires input of the spectral components, identified experimentally in Fig. 2d (see Supplementary Note 5 for the detailed fitting process and discussion). The deconvoluted absorbance intensities were converted to an area density of redox transitions using a potential step measurement in a single-redox transition regime, correlating the charge passed with the absorbance intensity according to the Lambert–Beer law (that is, the absorbance of an individual redox transition is considered to be linearly proportional to its density) (see Supplementary Figs. 19 and 20 for details). The densities of the redox transitions, obtained directly from deconvolutions, show typical sigmoid shapes with increasing potential (top panel of Fig. 3a), with similar densities of redox-active states participating in all three redox transition processes. The saturated density of redox transitions in IrO_x ($-3.5 \times 10^{16} \text{ cm}^{-2}$) is more than six times higher than that for IrO_2 ($-5.5 \times 10^{15} \text{ cm}^{-2}$) (top panel of Fig. 3b), which we attribute to the higher proton penetration in addition to the higher porosity within the structure. Assuming that the saturating densities of redox transitions observed in our spectro-electrochemical analyses indicate full coverage, the coverage θ of each

redox state at a given potential is defined as $\theta = D/D_{\text{max}}$, where D is the density of states and D_{max} is the maximum saturating density. Therefore, θ is a unitless value. Notably, the state generated from redox transition 3 does not saturate within the observed potential regime, and therefore the maximum density was assumed to be the same as redox transition 1 as both redox transitions occur on the same coordinatively unsaturated (CUS) site (see ‘DFT calculations’ in the Methods below).

The resulting coverage (θ) versus potential (U) data, that is, the electroadsorption isotherms, can be modelled using the Frumkin isotherm with coefficient of determination R^2 values as high as 0.99, as opposed to a simple Langmuir isotherm (dashed line in Fig. 3a (top panel); see Supplementary Note 6 and Supplementary Figs. 23 and 24 for details of the fitting). These excellent fits indicate the existence of lateral interactions between the redox states, as assumed in the Frumkin model. Similar Frumkin-type behaviour and the corresponding interaction has also been observed in the redox transitions of an amorphous cobalt oxide by Risch and co-workers³⁹. Mathematically, in a Frumkin electroadsorption model, the redox transition free energy $\Delta G_{\text{redox}}^0$ is a function of the redox-state coverage, that is, $\Delta G_{\text{redox}}^0(\theta) = \Delta G_{\text{redox}}^0(\theta=0) + r\theta$, where r (in electronvolts) is the interaction energy of the adsorbates at full coverage and θ is the coverage of the adsorbates ($0 < \theta < 1$). Analysing the θ – U data, we can obtain the value for the adsorbate–adsorbate interaction energy r . The fitted interaction energy r and the half-coverage potential $U_{(\theta=1/2)}$ for both amorphous and rutile iridium oxides are labelled in Fig. 3a,b. Interestingly, we found that the adsorbate–adsorbate interaction energy r values fitted from redox transition 3 on amorphous IrO_x and rutile IrO_2 are similar,

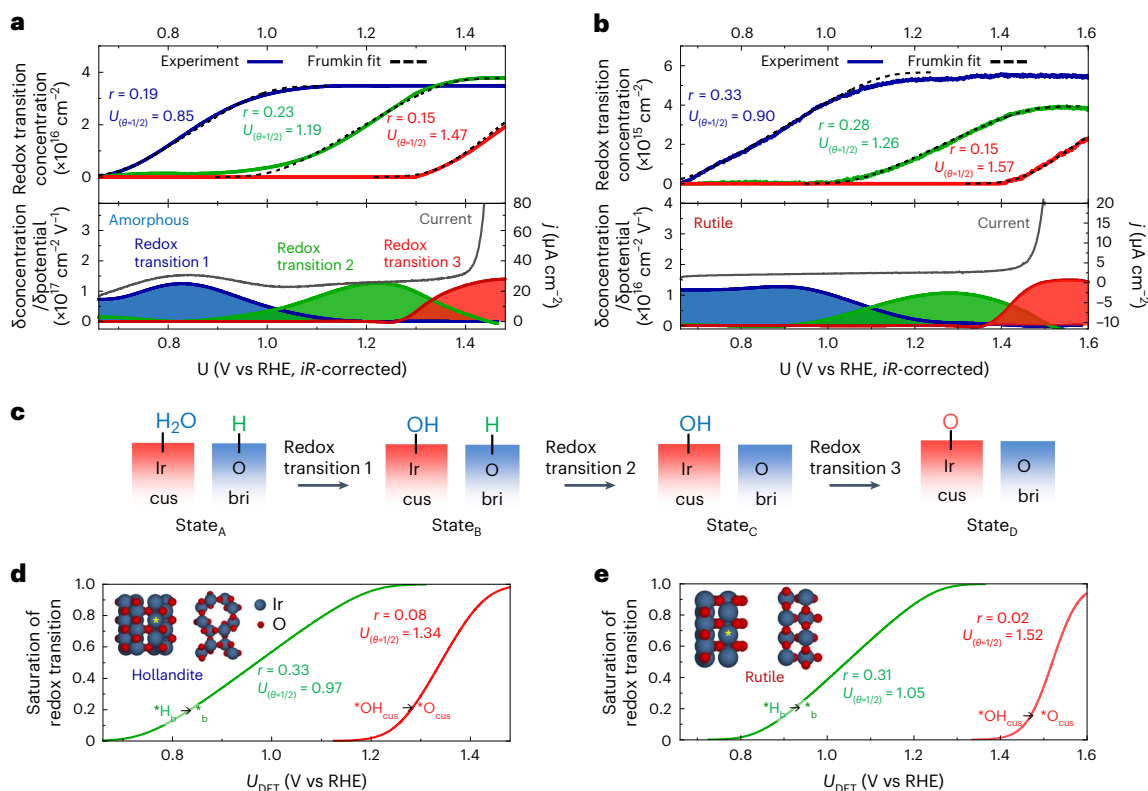


Fig. 3 | Redox transition densities as a function of potential in amorphous IrO_x and rutile IrO_2 . **a, b**, Densities of redox transitions for amorphous IrO_x (**a**) and rutile IrO_2 (**b**) that have occurred as a function of the potential (solid lines), and the corresponding Frumkin isotherm fitting results (dashed lines). The bottom panels show the derivatives of these redox transition densities with respect to the potential U , represented as redox transition waves. These redox waves are co-plotted with the linear scan voltammetry curves (grey line, right y axis) as a comparison between optically and electrochemically determined

redox transitions. j , current density. **c**, Schematic showing the proposed physical origin of the redox transitions and the redox states involved in these transitions on the basis of DFT calculations. **d, e**, DFT calculations for the saturation of $\text{OH}_{\text{cus}} + \text{*H}_b \rightarrow \text{*OH}_{\text{cus}} + \text{H}^+ + \text{e}^-$ and $\text{*OH}_{\text{cus}} \rightarrow \text{*O}_{\text{cus}} + \text{H}^+ + \text{e}^-$ transitions as a function of the potential U on hollandite iridium oxide (**d**) and rutile IrO_2 (**e**). The inset in **d** and **e** shows the hollandite IrO_2 (001) and rutile IrO_2 (110) surface structure, respectively. The coordinatively unsaturated iridium site is marked by the yellow asterisk.

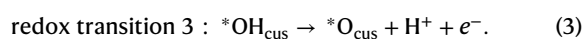
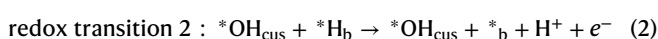
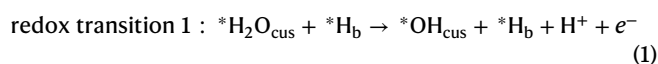
both at about 0.15 eV, indicating that the interaction strength between the adsorbates involved in this redox transition are similar despite the changes in the iridium coordination environment between the amorphous and crystalline iridium oxides. However, for surfaces with a substantially different surface structure and/or density of CUS sites, this interaction strength may differ.

The transient rate of potential-associated redox transitions is determined by the derivative of the density of redox transitions over the potential (Fig. 3a,b, bottom panels). The peak positions for redox transitions on the amorphous and crystalline iridium oxides, obtained from a deconvolution analysis of the optical signal, were found to be at about 0.82 and 0.90 V_{RHE} for redox transition 1, 1.22 and 1.26 V_{RHE} for redox transition 2 and 1.47 and 1.57 V_{RHE} for redox transition 3 (Supplementary Table 3 and Fig. 3a,b). These optically determined redox transition waves match well with the less-well-resolved redox transitions observed in the linear sweep voltammetry curves for amorphous IrO_x . In addition, the predicted linear sweep voltammetry curves from the redox transitions are comparable to the experimentally observed curve, in terms of both curve shape and amplitude for both the amorphous and crystalline iridium oxides (grey line in the bottom panel of Fig. 3a,b and in Supplementary Fig. 21). The positions of redox transition 1 and redox transition 2 are also in agreement with the redox peak positions on amorphous IrO_x and perovskite SrIrO_3 determined by Geiger et al. (both are at around 0.8 and 1.2 V)⁸. Notably, the redox current for redox transition 3, corresponding to the optical data at OER-relevant potentials, is masked by the OER current measured electrochemically in the cyclic voltammogram. A redox peak at a similar potential (1.63 V_{RHE}) has

also been observed by Kuo et al. on an IrO_2 (110) surface³⁰. It is clear that amorphous IrO_x undergoes the redox transition 3 process ($\sim 1.3 V_{\text{RHE}}$) at a potential approximately 100 mV lower than rutile IrO_2 ($\sim 1.4 V_{\text{RHE}}$; see Supplementary Fig. 22 for a direct comparison of the absorbance signals). This suggests that the differences in coordination between the iridium centres in amorphous and crystalline iridium oxides result in stronger binding of the oxygenated intermediates in IrO_x compared with IrO_2 .

The UV–visible absorbance changes in Fig. 2 can be assigned to changes in intervalence charge transfer within the iridium d orbitals, which correlates to the oxidation of iridium and the change of surface adsorbates coordinated to the iridium centre^{41–43}. Previous operando XAS studies have indicated that the first and second redox transitions in similar amorphous IrO_x may correspond to the $\text{Ir}^{3+}/\text{Ir}^{4+}$ and $\text{Ir}^{4+}/\text{Ir}^{5+}$ transitions^{44–46}, although a consensus on the exact oxidation state, especially during the OER, still has not been reached²⁷. In particular, in OER potential regions where redox transition 3 occurs, previous operando XAS or XPS studies have suggested the formation of Ir^{4+} (ref. 47), $\text{Ir}^{4.x+}$ (ref. 48) or Ir^{5+} species^{10,49,50}. Recent findings have suggested the formation of electrophilic oxygen species (O^{1-}) at OER-relevant potential regions^{20,21,26}. Whereas the precise iridium oxidation state on the surface remains under debate, the aforementioned literature suggest that the redox transitions involve adsorbed oxygenated species. To verify the nature of these surface adsorbates, we first use DFT calculations (see the computational methods in Methods and Supplementary Note 7). We then use the behaviour of these adsorbates to represent the redox transition process, which is intrinsically linked to changes in the iridium oxidation state. We model the rutile IrO_2 (110)

surface, which consists of rows of iridium atoms coordinated by bridging oxygens separated by rows of CUS sites (inset of Fig. 3e; see details in Supplementary Fig. 25). The adsorption of *H, *H₂O, *OH and *O on the CUS site and *H on the bridging oxygen (*H_b) was considered at full coverage. The calculations were performed at constant charge, and the computational hydrogen electrode⁵¹ was used to determine the most stable surface adsorbate structure at a given potential (Supplementary Fig. 26). The interaction between the adsorbates was explored by calculating the free energy of the stepwise transition between the most stable adsorbates in a unit cell with three CUS sites, that is, at different coverages of the species. For selected surfaces the OER was modelled, two different reaction pathways were considered as described in previous work⁵² (Supplementary Fig. 27). On the basis of these energies, the redox transition potential at half coverage $U_{(\theta=1/2)}$ and the interaction energy r were calculated and are plotted as adsorption isotherms in Fig. 3e. The calculated energies at half coverage for *OH (1.05 V_{DFT-RHE}) and *O (1.52 V_{DFT-RHE}) on the CUS site of rutile IrO₂ match well with experimental half-wave redox potentials for redox transition 2 (1.26 V_{RHE}) and redox transition 3 (1.57 V_{RHE}), considering the accuracy of DFT calculations^{53,54} (Supplementary Table 5). Our calculations are also in agreement with previous work, which attributed the redox transitions at around 1.20 V_{RHE} and 1.63 V_{RHE} on IrO₂(110) surfaces in 0.1 M HClO₄ to *OH and *O adsorption on the CUS site, respectively³⁰. Redox transition 1 was considered to be *H desorbing from the CUS site or *H₂O dissociating to form *OH on the CUS site, but the calculated potential values for both transitions (<0.19 V_{DFT-RHE}) do not match closely with the experimental result of 0.90 V_{RHE}, even if the possibility of an intermediate structure with some CUS sites covered by *H₂O is considered (see Supplementary Fig. 26 for details). This is to be expected as the rutile surface is at the limit of stability at this potential, and the number of possible surface structures thus becomes large. Given that the saturated densities of redox transitions 1 and 2 are relatively close (with a deviation of between 3 and 30%), we anticipate that all iridium CUS sites will participate in the first redox transition with the transfer of a single electron, similar to the other two redox transitions. The differences in the total saturated densities of redox transitions 1 and 2 can be attributed to the polycrystalline nature of the sample where surface facets with an unequal number of bridge and CUS sites may be exposed. Therefore, opting for the simplest possible assignment for redox transition 1, we attribute these redox transitions to:



where *__b represents the bridge oxygen adsorption site. The schematic in Fig. 3c shows the redox transitions and the redox states involved. The coverage of these redox states at CUS and bridge sites can be obtained using the fitted Frumkin isotherm and this DFT assignment (Supplementary Fig. 29). For amorphous IrO_x, the disordered surface structure cannot be modelled via periodic DFT calculations. Instead, as a representative of a more open IrO_x structure with a larger separation between the adsorbates, the (001) surface of hollandite IrO₂ is modelled, and calculations are carried out for the transitions OH_{CUS} + *H_b → *OH_{CUS} + *__b + H⁺ + e⁻ and *OH_{CUS} → *O_{CUS} + H⁺ + e⁻ (Fig. 3d)¹⁸. The energy values of redox transitions 2 (0.97 V_{DFT-RHE}) and 3 (1.34 V_{DFT-RHE}) on hollandite IrO_x are lower than on rutile IrO₂ (Supplementary Fig. 28), in agreement with our experimental observations.

Our DFT calculations also capture the interaction strength between *OH adsorbates on both the rutile and hollandite surfaces, showing that the calculated redox potential increases from 0.89 V_{DFT-RHE} at one-third coverage to 1.20 V_{DFT-RHE} at full coverage of *OH for the rutile

structure, and from 0.80 to 1.13 V_{DFT-RHE} for the hollandite structure (see Supplementary Note 8 for details of interaction parameter calculations). However, the interaction of *O cannot be fully captured using this model. The calculated interaction energies of *O are only about 0.02 and 0.08 eV for rutile and hollandite IrO₂, respectively, which are considerably lower than the experimentally observed value of 0.15 eV. This observation is in agreement with recent work suggesting that the repulsive interactions for *O species can only be captured by including solvent effects in the DFT model as the *O interactions may propagate through the water layer²⁶. Therefore, we hypothesize that these interactions between *O species are mediated by the electrolyte, as also suggested by the measurements of Hu et al. on well-defined single crystal RuO₂(110), where only surface ruthenium sites are active⁵⁵. The above experimental and theoretical results indicate the key role of repulsive interactions between the adsorbates, which give rise to the Frumkin electroadsorption isotherm (Fig. 3a,b) and change the free energy of elementary steps in the OER as a function of coverage.

Correlating accumulated *O_{CUS} active states with the OER

Next, we investigated the lifetime of these accumulated redox states and their correlation with the water oxidation reaction on IrO_x. We measured the decay kinetics of the accumulated states when the potential was released from an oxygen-evolving potential to an open-circuit potential using time-resolved UV–visible absorption spectroscopy (see Supplementary Note 9 for details of the decay kinetics measurements)^{28,37,56}. This experiment is shown in Fig. 4a, where two spectrally distinct decay phases were observed during open-circuit decay—a fast decay component (initial 1 s) with a dominant absorption decay peak at around 500 nm, and a slow decay component (100–200 s) with the maximum signal at around 800 nm (see Supplementary Note 9 and Supplementary Fig. 33 for detailed deconvolution of the decay data). The differential absorption spectra for these two phases are in excellent agreement with the differential absorption spectra of redox transition 3 and redox transition 2, respectively (Fig. 4b), indicating that the fast decay of absorbance arises primarily from the decay of state_b to state_c (that is, the decay of *O_{CUS}), whereas the slow decay arises mainly from the decay of state_c to state_b (that is, the decay of bridge oxygen O_{br}). Further comparison of the optical signal decay in different potential regimes shows that state_b (*OH_{CUS}) and state_c (O_{br}) remain stable even after the applied potential is switched off, indicating that these states are very stable once generated and will not be the catalytically relevant species (Supplementary Fig. 34). Conversely, the *O_{CUS} species decays rapidly once the applied potential is removed, indicating the reactivity of *O_{CUS} for forming molecular oxygen. Based on the established DFT calculations on IrO₂(110)^{26,57,58}, which suggest that the formation of *OOH from *O is the RDS, we interpret the fast decay process as described in Fig. 4c: a site in the active state (*O_{CUS}) proceeds along the reaction path via nucleophilic attack from a water molecule, forming the O–O bond and followed by the release of oxygen. Here, the charge is balanced by other active states through accepting a proton and becoming reduced to regenerate *OH_{CUS} on the surface (as no charge is passed through the external circuit during open-circuit conditions). To validate this decay mechanism, we measured oxygen using highly sensitive on-chip electrochemical mass spectrometry (EC-MS). This technique enables the in situ measurement of gas products during electrochemistry with a resolution down to subpicomole per second sensitivity^{59,60}. The net amount of O₂ produced during open-circuit decay from 1.46 to 1.40 V_{RHE}, detected using EC-MS, is -0.87 nmol cm⁻². This amount of oxygen is in good agreement with the O₂ release expected from decay of the accumulated *O_{CUS} from 1.46 to 1.40 V_{RHE} (0.70–0.96 nmol cm⁻²) (see supplementary Note 10 and Supplementary Fig. 37 for details). This analysis confirms that the decay of *O_{CUS} is coupled with O₂ release, with four *O_{CUS} atoms being consumed per molecule of O₂ generated. As a result, where τ is the time constant of this active-state decay, it implies an intrinsic rate for the RDS of 1/4 τ for O₂ released per second.

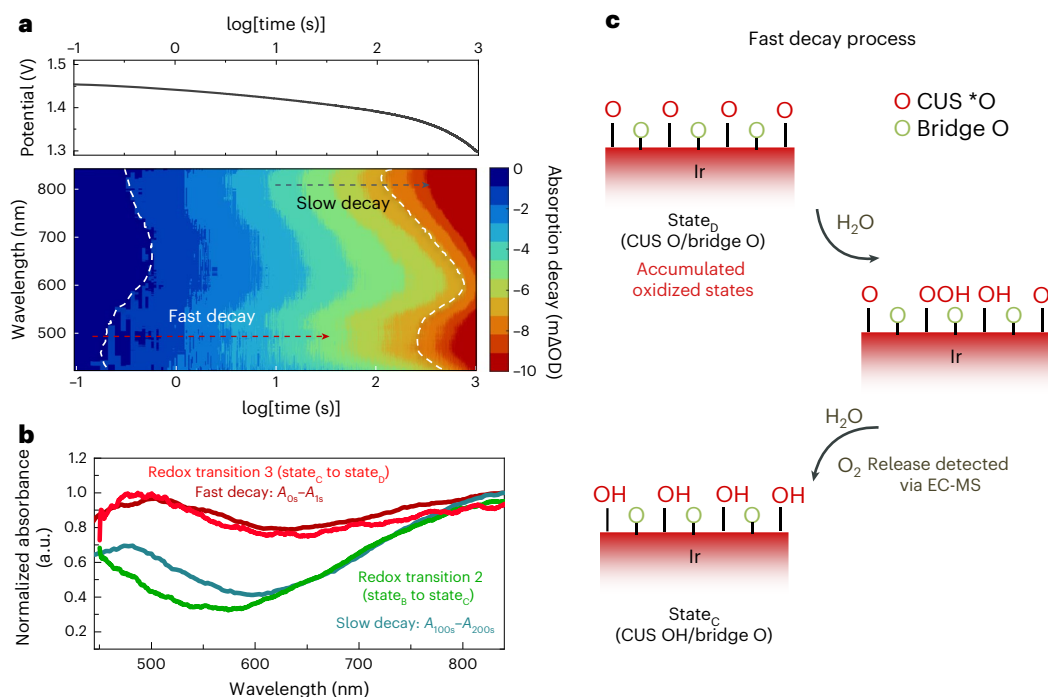


Fig. 4 | Active states for iridium oxides and their water oxidation mechanism.

a, Change in potential (versus RHE) during open-circuit decay (top) and the change in absorbance (A) as a function of time after beginning decay under open-circuit conditions (bottom). The changes in absorbance are calculated with respect to absorption immediately before turning to the open-circuit potential. The colour scale represents the decrease in absorbance compared with that before open-circuit decay. The white dashed lines denote the same levels of decay in absorption. At the initial time (1 s), the absorption decay is at a maximum at wavelengths of ~ 500 and ~ 800 nm, whereas after 100 s, the absorption decay

is dominant at ~ 800 nm. **b**, Comparison of the differential spectra obtained from the decay and redox transitions during linear sweep voltammetry. Spectra from the initial 1 s after the decay (dark red) and from 100–200 s after the decay (dark green) were obtained from Supplementary Fig. 33c. The spectral shape of redox transition 3 (light red) and redox transition 2 (light green) are from Fig. 2d. All spectra are normalized to their maximum absorbance for comparison. **c**, Proposed mechanism for the OER, involving the nucleophilic attack of water on the accumulated $^*O_{\text{CUS}}$ species to form molecular oxygen, corresponding to the fast decay phase in **a**, that is, the decay of state_b to state_c.

By varying the applied potential and probing the decay when the cell is switched to open circuit, we are able to control the density of $^*O_{\text{CUS}}$ and investigate its effect on the intrinsic rate of the RDS (a detailed measurement of τ and calculation of the intrinsic rate can be found in Supplementary Note 9 and Supplementary Figs. 35 and 36).

Determining the intrinsic water oxidation kinetics

Having confirmed that the optically detected accumulated $^*O_{\text{CUS}}$ are reactive towards O–O coupling and O₂ release, we explored how these active states control the reaction rate on amorphous IrO_x and rutile IrO₂. We used two methods to estimate the intrinsic rate of the RDS as a function of the potential (and thus as a function of the $^*O_{\text{CUS}}$ coverage). First, we normalized the O₂ generation rate (obtained from the current) to the density of $^*O_{\text{CUS}}$, the active states from which the RDS (that is, O–O bond formation) proceeds. Such an RDS on IrO₂ has also been supported by other literature reports^{25,26,57,58}. Second, we accessed the $^*O_{\text{CUS}}$ decay rate resulting from O–O bond formation using the previously described potential-decay measurement. The above two analyses yield the intrinsic rate of the RDS, which are described using TOF (O₂ per $^*O_{\text{CUS}}$ per s) and TOF_{decay}, respectively.

Figure 5a shows the active-state $^*O_{\text{CUS}}$ coverage and the intrinsic rate of the RDS for amorphous IrO_x and rutile IrO₂. We find that whereas rutile IrO₂ has fewer active states at a given potential, it has a similar intrinsic rate of the RDS as measured by the O₂ evolution rate and a slightly lower intrinsic rate of the RDS as measured via the open-circuit decay within the studied potential regime. At more positive potentials (thus higher current densities), the coverage of $^*O_{\text{CUS}}$ cannot be measured due to the impact of severe bubble formation on the optical signal. We thus extrapolated the activity per $^*O_{\text{CUS}}$ in the higher potential range using the measured current density at the higher potential

and an estimated coverage of $^*O_{\text{CUS}}$ from our Frumkin isotherm fitting results (Supplementary Fig. 39). We note that the TOF values obtained via both methods are in good agreement with those on mass-selected iridium oxide particles (which are presumably an amorphous/native oxide formed via the electrochemical oxidation of metallic iridium nanoparticles)⁶¹ (Supplementary Fig. 40). This notion is in agreement with recent work using the noise level from an electrochemical scanning tunnelling microscope to probe catalytic activity locally, which showed that the OER rates are similar on a film of amorphous IrO_x, with negligible surface sensitivity⁶². To further explore the view that most, if not all, redox-active sites are also active for the OER, we evaluated the TOF per redox-active centre by normalizing the current to the total integrated charge in the first redox transition for films of varying thicknesses (see Supplementary Note 11 and Supplementary Fig. 41 for a detailed discussion). We find that the TOF is independent of the thickness, which is consistent with the notion that the sites that are redox-active are also OER-active in the hydrated amorphous oxide materials, and the observed redox transition states are thus less likely to be related to Faradaic processes of bulk sites that do not participate directly in the OER. Dau and co-workers came to similar conclusions with thickness-independent TOF values on hydrous amorphous cobalt catalysts^{63–65}.

Given that the coverage of the adsorbates in the Frumkin isotherm plays a key role in the binding energetics of the adsorbates and thus controls the reactivity of the states, we next compare the TOF (O₂ per $^*O_{\text{CUS}}$ per s) and the TOF_{decay} for amorphous IrO_x and rutile IrO₂ as a function of the $^*O_{\text{CUS}}$ coverage (Fig. 5b). We note that for both iridium oxides, the logarithm of the TOF increases roughly linearly with the $^*O_{\text{CUS}}$ coverage in the observed range of coverage. This result is similar to the observation in a recent study by Nong et al.²⁶ where they found that

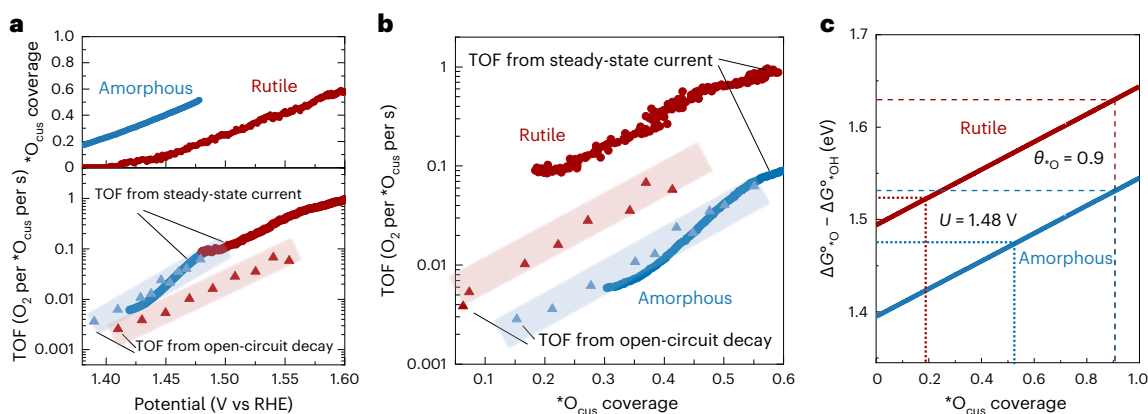


Fig. 5 | Intrinsic rate of the RDS for amorphous IrO_x and rutile IrO_2 . **a**, Coverage of $^*\text{O}_{\text{cus}}$ as a function of the potential for amorphous and rutile iridium oxides (top), and the corresponding TOF per active state of amorphous IrO_x and rutile IrO_2 at the same potential (bottom). **b**, Intrinsic reaction rate per active state of IrO_x and IrO_2 as a function of the coverage of $^*\text{O}_{\text{cus}}$. The red and blue shaded regions in **a** and **b** are guides for the eye. **c**, Experimentally determined $\Delta G^{\circ}_{\text{O}} - \Delta G^{\circ}_{\text{OH}}$ values at different coverages of $^*\text{O}_{\text{cus}}$. The $\Delta G^{\circ}_{\text{O}} - \Delta G^{\circ}_{\text{OH}}$ values are calculated following the Frumkin electroadsorption isotherm $\Delta G^{\circ}_{\text{O}} - \Delta G^{\circ}_{\text{OH}} = \Delta G^{\circ}_{\text{O}} - \Delta G^{\circ}_{\text{OH}}(\theta_{\text{O}} = 0) + r\theta_{\text{O}}$,

where $\Delta G^{\circ}_{\text{O}} - \Delta G^{\circ}_{\text{OH}}(\theta_{\text{O}} = 0)$ represents the binding energy of $^*\text{O}_{\text{cus}}$ assuming zero coverage, and r (in electronvolts) is the interaction energy of the adsorbates. The values of $\Delta G^{\circ}_{\text{O}} - \Delta G^{\circ}_{\text{OH}}(\theta_{\text{O}} = 0)$ and r were determined by fitting the electroadsorption isotherms in Fig. 3a,b. The dotted lines indicate the $\Delta G^{\circ}_{\text{O}} - \Delta G^{\circ}_{\text{OH}}$ values at the same potential of 1.48 V_{RHE} ($^*\text{O}_{\text{cus}}$ coverage values for IrO_x and IrO_2 are -0.51 and -0.19, respectively, as determined in Fig. 5a), whereas the dashed lines indicate $\Delta G^{\circ}_{\text{O}} - \Delta G^{\circ}_{\text{OH}}$ at a constant $^*\text{O}_{\text{cus}}$ coverage of 0.9 for each of the iridium oxides (see Supplementary Note 6 for details).

the log(current) increases linearly with the total charge, and suggested from DFT that the activation energy of the RDS decreases linearly with the increase in $^*\text{O}_{\text{cus}}$ coverage because of the long-range interactions between the $^*\text{O}$ species. Combining experimental and DFT calculation results, they suggested a chemical RDS for the OER on iridium oxides. Here, by experimentally tracking the intrinsic rate of the RDS as a function of the $^*\text{O}_{\text{cus}}$ coverage, we observe similar results. We also note that the slope values of $\log(\text{TOF}_{\text{decay}})$ versus $^*\text{O}_{\text{cus}}$ coverage in Fig. 5b are similar for amorphous IrO_x and rutile IrO_2 , which is consistent with our observation that they have similar adsorbate–adsorbate interaction energies r . The repulsive interaction observed here between oxo species causes a destabilization of the adsorbed $^*\text{O}_{\text{cus}}$ species (that is, $\Delta G^{\circ}_{\text{O}} - \Delta G^{\circ}_{\text{OH}}$ becomes larger), thus reducing the free energy of the RDS (O–O bond formation from $^*\text{O}_{\text{cus}}$). This suggests that the concentration of active species not only increases the reaction rate, by providing more sites where the reaction can occur, but also increases the rate by increasing the driving force or decreasing the reaction barrier caused by the change in chemical potential of these active species.

From Fig. 5b, it is also apparent that, at the same $^*\text{O}_{\text{cus}}$ coverage, the intrinsic activity of the RDS on rutile IrO_2 is around one order of magnitude higher (as measured by TOF (O_2 per $^*\text{O}_{\text{cus}}$ per s)) and factor of five higher (as measured by $\text{TOF}_{\text{decay}}$) than on amorphous IrO_x . We rationalize this difference in activity to the potential-dependent binding energetics of $^*\text{O}_{\text{cus}}$. From the experimentally observed energetics of $^*\text{O}_{\text{cus}}$, the values of $\Delta G^{\circ}_{\text{O}} - \Delta G^{\circ}_{\text{OH}}$ at $^*\text{O}_{\text{cus}}(\theta_{\text{O}} = 0)$ for rutile IrO_2 is around 0.1 eV larger than that of amorphous IrO_x (that is, an extra 0.1 V is required to form $^*\text{O}_{\text{cus}}$ on rutile IrO_2), and the values for both increase with $^*\text{O}_{\text{cus}}$ coverage at a slope of roughly 0.15 eV per coverage increment due to the similar Frumkin interaction strengths (Fig. 5c). As a result, at a constant coverage of $^*\text{O}_{\text{cus}}$, compared with amorphous IrO_x , rutile IrO_2 binds oxygen more weakly, which facilitates O–O bond formation from $^*\text{O}_{\text{cus}}$ in the RDS, leading to a higher intrinsic activity per active state. On the other hand, at a constant potential, for example, at 1.48 V_{RHE} , this binding energy difference decreases to around 0.05 eV because amorphous IrO_x has a higher coverage of $^*\text{O}_{\text{cus}}$ at this potential, thus weakening the $^*\text{O}_{\text{cus}}$ binding more greatly. Therefore, the intrinsic activity at a constant potential is similar, and the order of magnitude greater geometric-area-normalized current density observed for amorphous IrO_x is mainly because it has a higher density of active states, as shown in Fig. 3a,b.

Design principles for highly active OER catalysts

The potential (and coverage) dependence of the intrinsic water oxidation kinetics determined herein show the importance of the adsorbate–adsorbate interactions in controlling the OER kinetics. The conventional approach for catalyst design has focused on developing catalysts with optimal binding energetics ($\Delta G^{\circ}_{\text{O}} - \Delta G^{\circ}_{\text{OH}}$) that correspond to -1.6 eV (refs. 24,25,58). This implicitly assumes that this value is independent of the coverage. Here we have clearly experimentally demonstrated the weakening of the $^*\text{O}$ binding energy with increasing coverage. This indicates that optimal binding energetics can also be obtained on surface sites that are strongly binding at low coverage ($\Delta G^{\circ}_{\text{O}} - \Delta G^{\circ}_{\text{OH}} < 1.6$ eV at $\theta_{\text{O}} \approx 0$) but have strong repulsive interactions, which weaken the $^*\text{O}$ binding energies at high coverage, thereby enabling these sites to achieve the optimal $\Delta G^{\circ}_{\text{O}} - \Delta G^{\circ}_{\text{OH}}$ values under reaction conditions that correspond to higher coverage.

To include the influence of adsorbate–adsorbate interactions on $\Delta G^{\circ}_{\text{O}} - \Delta G^{\circ}_{\text{OH}}$ values, and thus the intrinsic activity per state, we construct a new three-dimensional volcano plot. This volcano plot can be seen as a deconvolution of the previous descriptor $\Delta G^{\circ}_{\text{O}} - \Delta G^{\circ}_{\text{OH}}$ into two components: the binding energetics on a surface with zero $^*\text{O}$ coverage ($\Delta G^{\circ}_{\text{O}} - \Delta G^{\circ}_{\text{OH}}(\theta_{\text{O}} = 0)$), and the interaction strength between $^*\text{O}$ species, following a Frumkin-isotherm-related equation ($\Delta G^{\circ}_{\text{O}} - \Delta G^{\circ}_{\text{OH}} = \Delta G^{\circ}_{\text{O}} - \Delta G^{\circ}_{\text{OH}}(\theta_{\text{O}} = 0) + r\theta_{\text{O}}$). The relative activity per state is represented by the thermodynamic overpotential of the OER on the active state, and is calculated from the absolute difference between the $\Delta G^{\circ}_{\text{O}} - \Delta G^{\circ}_{\text{OH}}$ value of the catalysts and the predicted optimal value of 1.60 eV (that is, relative activity = $|\Delta G^{\circ}_{\text{O}} - \Delta G^{\circ}_{\text{OH}} - 1.6$ eV|), as reported in the studies of Rossmeisl, Nørskov and colleagues^{24,25}. We first construct this plot assuming a near-saturated coverage, $\theta_{\text{O}} = 0.9$. As shown in Fig. 6a, the optimal activity of the states can be achieved either via optimal $^*\text{O}$ binding at low coverage without any $^*\text{O}$ interaction (that is, $\Delta G^{\circ}_{\text{O}} - \Delta G^{\circ}_{\text{OH}} \approx 1.6$ eV at $\theta_{\text{O}} \approx 0$, $r = 0$ eV), which is the top of a conventional volcano plot, or via a stronger than optimal $^*\text{O}$ binding and strong interaction (for example, $\Delta G^{\circ}_{\text{O}} - \Delta G^{\circ}_{\text{OH}} = 1.0$ eV at $\theta_{\text{O}} \approx 0$, $r \approx 0.7$ eV). In the latter case, although each state binds $^*\text{O}$ much more strongly than optimal at zero coverage, the strong interaction strength results in weaker binding and optimum $\Delta G^{\circ}_{\text{O}} - \Delta G^{\circ}_{\text{OH}}$ at high coverage.

We note that the applied potentials to achieve the same coverage are different for catalysts with different $\Delta G^{\circ}_{\text{O}} - \Delta G^{\circ}_{\text{OH}}(\theta_{\text{O}} = 0)$ and r values. To include both potential and coverage effects, we construct a

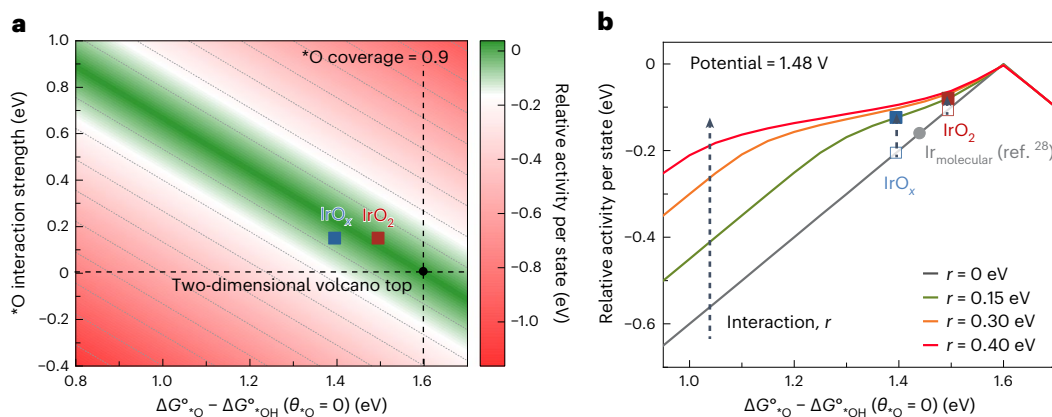


Fig. 6 | Effects of the *O interaction strength and *O binding energetics on the intrinsic activity per active state. a, Contour plot of relative activity as a function of the free energy of *O relative to *OH at an *O coverage of zero. The corresponding positions for amorphous IrO_x and rutile IrO₂ on the plot at a near-saturated coverage ($\theta_{\text{O}} = 0.9$) have been denoted. The relative activity is evaluated via the thermodynamic overpotential, which is calculated as the absolute difference between the energetic $\Delta G^{\circ}_{\text{*O}} - \Delta G^{\circ}_{\text{*OH}}$ and the theoretical optimal value of 1.6 eV (that is, relative

activity = $-\Delta G^{\circ}_{\text{*O}} - \Delta G^{\circ}_{\text{*OH}} (\theta_{\text{O}} = 0.9) - 1.6$ eV); the smaller the difference, the higher the value, and the higher the activity is expected to be^{24,25,58}. **b**, Relative activity per active state at a potential of 1.48 V_{RHE} and the corresponding positions for amorphous IrO_x and rutile IrO₂ as well as a previously reported molecular iridium catalyst (assuming a mid-wave potential at -1.44 V_{RHE} given that no interaction (that is, $r = 0$) is observed)²⁸. The coverage of active states was obtained by numerically solving the Frumkin isotherm equation for given values of r and $\Delta G^{\circ}_{\text{*O}} - \Delta G^{\circ}_{\text{*OH}} (\theta_{\text{O}} = 0)$.

volcano plot at a fixed overpotential of 250 mV (Fig. 6b and Supplementary Fig. 42). The steep part of the left side of the volcano (for example, when $\Delta G^{\circ}_{\text{*O}} - \Delta G^{\circ}_{\text{*OH}} (\theta_{\text{O}} = 0) < 1.28$ eV in the curve of $r = 0.15$ eV) is where the *O coverage is saturated, whereas the less steep part represents where $\Delta G^{\circ}_{\text{*O}} - \Delta G^{\circ}_{\text{*OH}} (\theta_{\text{O}})$ is changing due to the Frumkin repulsion term. The Frumkin repulsion term has a higher impact on increasing the activity for a material with a stronger *O binding energy, for a given interaction strength. This is evident from our data on amorphous and rutile iridium oxide catalysts, where the adsorbate–adsorbate interaction increases the relative activity of the two materials by different degrees, although they have a similar interaction parameter (-0.15 eV). This is because the stronger binding strength of *O on the IrO_x surface results in a higher coverage for IrO_x compared with IrO₂ at this potential (Fig. 5a, top panel), and a consequently higher repulsion between adsorbates. However, both show a higher activity than the molecular iridium catalyst analysed previously, which has no adsorbate–adsorbate interaction²⁸. This observation is consistent with our previous suggestion that, although the studied molecular iridium catalyst showed faster kinetics than amorphous IrO_x at low overpotentials, it is less active than amorphous IrO_x at higher overpotentials due to a lack of cooperative interactions between active states²⁸. Similar analyses at overpotentials of 200 and 280 mV are also given in Supplementary Fig. 43. These results indicate that the potential can alter the coverage of *O species, which in turn can weaken the binding energies for catalysts that bind oxygen too strongly in a conventional volcano plot, hence improving the OER activity. This analysis elucidates the fundamental origin of the activity discrepancies between different iridium-based catalysts, including amorphous and crystalline iridium oxides.

Conclusions

In conclusion, our work combines experimental and theoretical techniques to re-evaluate the design principles for water oxidation catalysts by unravelling the role of active sites in terms of their density, ordering and interactions between them on the reaction rate. Here we have resolved the formation of the redox centres in amorphous IrO_x and crystalline IrO₂ as a function of the potential, using time-resolved UV–visible spectroelectrochemistry and as a function of depth using ToF-SIMS combined with deuterium labelling. We also used DFT to provide a molecular-level interpretation of our results. From DFT, we assign the third spectral redox wave (redox transition 3) to the change

of *OH to *O on the Ir_{cus} site in both catalysts; in addition, the experimentally obtained O₂ evolution kinetics show an exponential dependence on the coverage of the species *O, corroborating predictions from earlier DFT-based models that O–O bond formation controls the reaction rate^{24–26}.

Our potential-decay results reveal that the intrinsic kinetics of O₂ evolution, that is, the reactivity of active *O states for O–O bond formation, are comparable, or slightly faster, on amorphous IrO_x compared with crystalline IrO₂ at a given potential in the studied potential regime; however, the greater penetration and hence density of sites per unit geometric area of redox centres in amorphous IrO_x, as measured using both optical spectroscopy and ToF-SIMS, account for the substantially higher geometric current density observed in this catalyst compared with crystalline IrO₂. Amorphous IrO_x binds more strongly to *O than to crystalline IrO₂ at low coverage; nonetheless, under the same potential for the reaction conditions, the coverage of *O is much higher than that of crystalline IrO₂, leading to greater weakening of *O as a result of repulsive adsorbate–adsorbate interactions. These two opposing effects lead to comparable intrinsic reaction rates on the two types of iridium under study. On the basis of these insights, we may expect that nanocrystalline iridium-based catalysts, which exhibit the high stability^{8,32} and intrinsic rate of rutile IrO₂ but with the high site density of amorphous IrO_x, will provide an optimal performance for O₂ evolution.

Beyond iridium oxides, our work highlights the role of adsorbate–adsorbate interactions on water oxidation catalysis; they are particularly important for catalysts on the strong binding side of the oxygen evolution volcano, such as with non-precious metal oxide MnO_x (ref. 25). Our work leads to a more accurate description of water oxidation kinetics than conventional models that are based solely on the binding energetics at zero coverage; moreover, it provides an additional, unexplored lever to aid the discovery of more active catalysts.

Methods

Synthesis of amorphous IrO_x and crystalline IrO₂

Amorphous IrO_x was prepared using an electrodeposition method analogous to previous reports^{27,31}. Typically, a solution with an iridium source was prepared by dissolving IrCl₃ hydrate (0.2 mmol; Fluorochem) and oxalic acid dihydrate (1 mmol; Sigma Aldrich) in water (30 ml). The pH was adjusted to 10 with K₂CO₃ (5 mmol; Sigma Aldrich,

≥99.0%). The volume of the solution was then increased to 50 ml by adding more water (20 ml). The solution was left to rest for four days at 35 °C and then stored in a refrigerator at 4 °C. The electrodeposition of IrO_x was conducted with a typical three-electrode set-up using this solution. A clean FTO glass substrate was used as the working electrode, and a platinum mesh and Ag/AgCl were used as the counter and reference electrodes, respectively. Polyimide tape was attached to the FTO surface to limit the conductive surface to 1 × 1 cm. The electrodeposition was carried out by applying an anodic current density of 35 μA cm⁻² for 1,000 s. The mass loading of the obtained IrO_x was around 80 μg cm⁻². For ToF-SIMS and XPS measurements, IrO_x was deposited on a titanium substrate for a longer deposition time of 12,000 s to obtain a thicker layer sample. SEM images were obtained from the sample deposited on both titanium substrates and FTO substrates. Rutile IrO₂ is obtained via thermal annealing of the IrO_x sample in the atmosphere at 550 °C for 8 h, at a heating rate of 10 °C min⁻¹. Thus, rutile IrO₂ sample has the same iridium mass loading as the amorphous IrO_x sample.

Characterization of materials

SEM images were obtained using a LEO 1525 scanning electron microscope (FESEM, 5 kV). X-ray diffraction measurements were carried out to determine the phase composition of each catalyst, and were obtained using a Bruker-Axs diffractometer equipped with a PSD LinXEye detector. The X-ray diffraction patterns were collected in the range of $10 \leq 2\theta \leq 70$ with a step size of 0.05°. XPS spectra were obtained using a Thermo Scientific K-Alpha spectrometer equipped with an aluminium K α X-ray source (1,486.6 eV) coupled with a 180° double-focusing hemispherical analyser with a 2 s detector at an operating pressure of 1×10^{-8} mbar and a flood gun to minimize charging effects from photoemission. The iridium L₃-edge XAS data were collected using the B18 beamline at Diamond Light Source, United Kingdom. The beamline has an energy range of 2.05–35 keV for spectroscopy. The energy of the incident X-ray beam was selected using a Si(111) monochromator, with a resolving power of $\lambda/\Delta\lambda \approx 5,000$. The XAS measurements for amorphous IrO_x and rutile IrO₂ were performed in fluorescence. The XAS measurements for standard sample iridium powder, IrCl₃ and IrO₂ (Alfa Sigma) were carried out in transmission mode.

Electrochemical measurements

All electrochemical measurements were carried out in 0.1 M HClO₄ prepared by dilution of concentrated perchloric acid (Suprapur 70% HClO₄, Merck) in ultrapure water (>18.2 MΩ cm, Sartorius). The electrochemical tests were conducted using a typical three-electrode set-up with an SP-150 or an SP-300 BioLogic potentiostat. The iridium oxides deposited on the FTO substrate (1 × 1 cm) were used directly as the working electrode. A platinum mesh and an Ag/AgCl electrode (KCl-saturated) were used as the counter and reference electrodes, respectively. The reference electrode was calibrated to the RHE in the same electrolyte using saturated H₂ on a clean platinum surface. Potentials were iR-compensated by manually subtracting the product of current and resistance $i \times R_u$, for which the resistance R_u (~25 Ω) was obtained from a high-frequency intercept of the real resistance during electrochemical impedance spectroscopy.

ToF-SIMS

ToF-SIMS measurements were performed using an IONTOF ToF-SIMS V instrument, with a sputter current of 75 nA. Bismuth ions were used as the primary analysis ion and 1 keV caesium ions were used as the sputter beam. The sputter beam was set to create a crater with a length and width of 300 μm. A square analysis area, with sides of 100 μm, was then set around the centre of the crater. Data were obtained over a mass range from mass-to-charge ratios (m/z) of 0–200 for negative secondary ions. Calibration was performed using C⁻, CH⁻, CH₂⁻, CH₃⁻, O⁻, OH⁻, F⁻ and ³⁵Cl⁻. The differences between the expected and observed masses after calibration were less than 50 ppm. The samples were

first electrochemically cycled in deuterated 0.1 M HClO₄ electrolyte and then subjected to ToF-SIMS to record the deuterium signal over the sputtering time.

Operando UV–visible absorption spectroscopy

Operando UV–visible absorption spectroscopy measurements were conducted in transmission mode. A stabilized 10 mW tungsten–halogen light source (SLS201L, Thorlabs) was used with a collimating package (SLS201C, Thorlabs). The light emitted from the lamp was transmitted through the sample and collected using a 1 cm diameter liquid light guide (Edmund Optics). Light transmitted to the spectrograph was first columnated and refocused using two 5 cm planoconvex lenses (Edmund Optics) to optimally match the optical components of the spectroscopy (Kymera 193i, Andor) and charge-coupled device (CCD) camera (iDus Du420A-BEX2-DD, Andor). The detector was maintained at –80 °C during the measurements to reduce the dark current and ensure a high signal-to-noise ratio. An Ivium Vertex potentiostat was used for electrochemical measurements, where data acquisition of both the electrochemical signal (that is, the potential and current) and the optical signal is facilitated using custom-built LabVIEW⁶⁶ software (see details in the Code availability statement). This custom-built software also ensures that the two signal sources match in the same time stamp. The measurements were carried out in potentiostatic mode, with a potential step and equilibration time equal to that for typical CV at a scan rate of around 1 mV s⁻¹. At each potential, 30 averages of the spectra were obtained (where each spectral acquisition takes ~30 ms), before moving to the next potential.

DFT calculations

All DFT calculations were performed using the grid-based projector augmented wave software package^{67,68}. The atomic simulation environment was used to set up and control the calculations⁶⁹. The calculations were performed with a plane-wave basis with an energy cut-off of 500 eV. The revised Perdew–Burke–Ernzerhof functional was used to describe the effects of exchange and correlation⁷⁰.

The (110) surface of rutile IrO₂ was modelled as a 3 × 1 slab with four atomic layers, of which two were fixed in the bulk geometry at the computationally optimized lattice constants ($a = 4.59$ Å and $c = 3.19$ Å, which compare well with experimental values of $a = 4.50$ Å and $c = 3.15$ Å)⁷¹. Twenty ångströms of vacuum separated the periodic images of the slab, and a dipole correction was used to decouple the electrostatic interactions on either side of the slab. The Brillouin zone was sampled using $4 \times 4 \times k$ -points.

The surface of amorphous IrO₂ cannot be modelled via periodic DFT calculations; however, to gain an understanding of the differences between rutile and amorphous IrO₂ we modelled the (001) surface of IrO₂ in the hollandite structure. This surface bears similarity to the rutile (110) surface; however, adsorbates are further separated (in the x direction) and the bulk is more open, as would be expected for an amorphous structure (see Supplementary Fig. 25 for a comparison of the two surfaces). This surface is modelled as a 3 × 1 slab with six atomic layers (three frozen), corresponding to 1.5 repeats of the unit cell, and sampled using $3 \times 4 \times k$ -points. The calculated lattice constants are $a = 10.13$ Å and $c = 3.18$ Å, which compare well with the experimental data of hollandite-type K_xIrO₂ ($a = 10.02$ Å, $b = 3.15$ Å, $c = 10.05$ Å and $\beta = 90.11^\circ$)⁷².

Data availability

The data that support the findings of this study are available within the main text and Supplementary Information. DFT optimized structures are available from <https://nano.ku.dk/english/research/theoretical-electrocatalysis/katlabdb/water-oxidation-activity-of-iridium-oxides/>. Data are also available from the corresponding authors upon reasonable request. Source data are provided with this paper.

Code availability

Scripts used for spectroelectrochemical data analysis are openly available at https://github.com/Caiwu-L/Paper_amorphous-IrOx_vs_Rutile_IrO2. Details of the home-built spectroelectrochemistry set-up and the LabView-based software are openly available at <https://opensourcespectroscopy.com/>. Python scripts used to analyse the DFT data are available from <https://nano.ku.dk/english/research/theoretical-electrocatalysis/katlabdb/water-oxidation-activity-of-iridium-oxides/>.

References

- Bernt, M. et al. Current challenges in catalyst development for PEM water electrolyzers. *Chem. Ing. Tech.* **92**, 31–39 (2020).
- Carmo, M., Fritz, D. L., Mergel, J. & Stolten, D. A comprehensive review on PEM water electrolysis. *Int. J. Hydrogen Energy* **38**, 4901–4934 (2013).
- Reier, T., Nong, H. N., Teschner, D., Schlögl, R. & Strasser, P. Electrocatalytic oxygen evolution reaction in acidic environments – reaction mechanisms and catalysts. *Adv. Energy Mater.* **7**, 1601275 (2017).
- Vesborg, P. C. & Jaramillo, T. F. Addressing the terawatt challenge: scalability in the supply of chemical elements for renewable energy. *RSC Adv.* **2**, 7933–7947 (2012).
- Wei, C. et al. Recommended practices and benchmark activity for hydrogen and oxygen electrocatalysis in water splitting and fuel cells. *Adv. Mater.* **31**, 1806296 (2019).
- Kasian, O., Grote, J.-P., Geiger, S., Cherevko, S. & Mayrhofer, K. J. J. The common intermediates of oxygen evolution and dissolution reactions during water electrolysis on iridium. *Angew. Chem. Int. Ed.* **57**, 2488–2491 (2018).
- Bernt, M., Siebel, A. & Gasteiger, H. A. Analysis of voltage losses in PEM water electrolyzers with low platinum group metal loadings. *J. Electrochem. Soc.* **165**, F305 (2018).
- Geiger, S. et al. The stability number as a metric for electrocatalyst stability benchmarking. *Nat. Catal.* **1**, 508–515 (2018).
- Gao, J. et al. Breaking long-range order in iridium oxide by alkali ion for efficient water oxidation. *J. Am. Chem. Soc.* **141**, 3014–3023 (2019).
- Nong, H. N. et al. A unique oxygen ligand environment facilitates water oxidation in hole-doped IrNiO_x core-shell electrocatalysts. *Nat. Catal.* **1**, 841–851 (2018).
- Reier, T. et al. Molecular insight in structure and activity of highly efficient, low-Ir Ir–Ni oxide catalysts for electrochemical water splitting (OER). *J. Am. Chem. Soc.* **137**, 13031–13040 (2015).
- Sun, W., Song, Y., Gong, X.-Q., Cao, L.-M. & Yang, J. Hollandite structure K_{x=0.25}IrO₂ catalyst with highly efficient oxygen evolution reaction. *ACS Appl. Mater. Interfaces* **8**, 820–826 (2016).
- Seitz, L. C. et al. A highly active and stable IrO_x/SrIrO₃ catalyst for the oxygen evolution reaction. *Science* **353**, 1011–1014 (2016).
- Diaz-Morales, O. et al. Iridium-based double perovskites for efficient water oxidation in acid media. *Nat. Commun.* **7**, 12363 (2016).
- Wan, G. et al. Amorphization mechanism of SrIrO₃ electrocatalyst: how oxygen redox initiates ionic diffusion and structural reorganization. *Sci. Adv.* **7**, eabc7323 (2021).
- Elmaalouf, M. et al. The origin of the high electrochemical activity of pseudo-amorphous iridium oxides. *Nat. Commun.* **12**, 3935 (2021).
- Abbott, D. F. et al. Iridium oxide for the oxygen evolution reaction: correlation between particle size, morphology, and the surface hydroxo layer from operando XAS. *Chem. Mater.* **28**, 6591–6604 (2016).
- Willinger, E., Massué, C., Schlögl, R. & Willinger, M. G. Identifying key structural features of IrO_x water splitting catalysts. *J. Am. Chem. Soc.* **139**, 12093–12101 (2017).
- Pfeifer, V. et al. The electronic structure of iridium oxide electrodes active in water splitting. *Phys. Chem. Chem. Phys.* **18**, 2292–2296 (2016).
- Pfeifer, V. et al. In situ observation of reactive oxygen species forming on oxygen-evolving iridium surfaces. *Chem. Sci.* **8**, 2143–2149 (2017).
- Pfeifer, V. et al. Reactive oxygen species in iridium-based OER catalysts. *Chem. Sci.* **7**, 6791–6795 (2016).
- Bockris, J. M. Kinetics of activation controlled consecutive electrochemical reactions: anodic evolution of oxygen. *J. Chem. Phys.* **24**, 817–827 (1956).
- Bockris, J. O. M. & Otagawa, T. The electrocatalysis of oxygen evolution on perovskites. *J. Electrochem. Soc.* **131**, 290 (1984).
- Man, I. C. et al. Universality in oxygen evolution electrocatalysis on oxide surfaces. *ChemCatChem* **3**, 1159–1165 (2011).
- Rossmesl, J., Qu, Z. W., Zhu, H., Kroes, G. J. & Nørskov, J. K. Electrolysis of water on oxide surfaces. *J. Electroanal. Chem.* **607**, 83–89 (2007).
- Nong, H. N. et al. Key role of chemistry versus bias in electrocatalytic oxygen evolution. *Nature* **587**, 408–413 (2020).
- Bozal-Ginesta, C. et al. Redox-state kinetics in water-oxidation IrO_x electrocatalysts measured by operando spectroelectrochemistry. *ACS Catal.* **11**, 15013–15025 (2021).
- Bozal-Ginesta, C. et al. Spectroelectrochemistry of water oxidation kinetics in molecular versus heterogeneous oxide iridium electrocatalysts. *J. Am. Chem. Soc.* **144**, 8454–8459 (2022).
- Gallagher, J. Co-operating to oxidize water. *Nat. Energy* **7**, 471 (2022).
- Kuo, D. Y. et al. Influence of surface adsorption on the oxygen evolution reaction on IrO₂(110). *J. Am. Chem. Soc.* **139**, 3473–3479 (2017).
- Petit, M. A. & Plichon, V. Anodic electrodeposition of iridium oxide films. *J. Electroanal. Chem.* **444**, 247–252 (1998).
- Geiger, S. et al. Activity and stability of electrochemically and thermally treated iridium for the oxygen evolution reaction. *J. Electrochem. Soc.* **163**, F3132 (2016).
- Hadden, J. H. L., Ryan, M. P. & Riley, D. J. Is nickel hydroxide charging only skin-deep? *ACS Appl. Energy Mater.* **3**, 2803–2810 (2020).
- Li, T. et al. Atomic-scale insights into surface species of electrocatalysts in three dimensions. *Nat. Catal.* **1**, 300–305 (2018).
- Kasian, O. et al. Degradation of iridium oxides via oxygen evolution from the lattice: correlating atomic scale structure with reaction mechanisms. *Energy Environ. Sci.* **12**, 3548–3555 (2019).
- Görlin, M. et al. Tracking catalyst redox states and reaction dynamics in Ni–Fe oxyhydroxide oxygen evolution reaction electrocatalysts: the role of catalyst support and electrolyte pH. *J. Am. Chem. Soc.* **139**, 2070–2082 (2017).
- Rao, R. R. et al. Spectroelectrochemical analysis of the water oxidation mechanism on doped nickel oxides. *J. Am. Chem. Soc.* **144**, 7622–7633 (2022).
- Francàs, L. et al. Spectroelectrochemical study of water oxidation on nickel and iron oxyhydroxide electrocatalysts. *Nat. Commun.* **10**, 5208 (2019).
- Risch, M. et al. Water oxidation by amorphous cobalt-based oxides: in situ tracking of redox transitions and mode of catalysis. *Energy Environ. Sci.* **8**, 661–674 (2015).
- Mom, R. V. et al. Operando structure–activity–stability relationship of iridium oxides during the oxygen evolution reaction. *ACS Catal.* **12**, 5174–5184 (2022).
- Frame, F. A. et al. Photocatalytic water oxidation with nonsensitized IrO₂ nanocrystals under visible and UV light. *J. Am. Chem. Soc.* **133**, 7264–7267 (2011).
- Ooka, H. et al. Legitimate intermediates of oxygen evolution on iridium oxide revealed by in situ electrochemical evanescent wave spectroscopy. *Phys. Chem. Chem. Phys.* **18**, 15199–15204 (2016).

43. Ooka, H., Takashima, T., Yamaguchi, A., Hayashi, T. & Nakamura, R. Element strategy of oxygen evolution electrocatalysis based on in situ spectroelectrochemistry. *Chem. Commun.* **53**, 7149–7161 (2017).
44. Mo, Y. et al. In situ iridium L_{II} -edge X-ray absorption and surface enhanced raman spectroscopy of electrodeposited iridium oxide films in aqueous electrolytes. *J. Phys. Chem. B* **106**, 3681–3686 (2002).
45. Minguzzi, A. et al. Easy accommodation of different oxidation states in iridium oxide nanoparticles with different hydration degree as water oxidation electrocatalysts. *ACS Catal.* **5**, 5104–5115 (2015).
46. Hüppauff, M. & Lengeler, B. Valency and structure of iridium in anodic iridium oxide films. *J. Electrochem. Soc.* **140**, 598–602 (1993).
47. Saveleva, V. A. et al. Operando evidence for a universal oxygen evolution mechanism on thermal and electrochemical iridium oxides. *J. Phys. Chem. Lett.* **9**, 3154–3160 (2018).
48. Hillman, A. R., Skopek, M. A. & Gurman, S. J. X-ray spectroscopy of electrochemically deposited iridium oxide films: detection of multiple sites through structural disorder. *Phys. Chem. Chem. Phys.* **13**, 5252–5263 (2011).
49. Diklić, N. et al. Surface Ir^{+5} formation as a universal prerequisite for O_2 evolution on Ir oxides. *ACS Catal.* **13**, 11069–11079 (2023).
50. Velasco-Vélez, J.-J. et al. Surface electron-hole rich species active in the electrocatalytic water oxidation. *J. Am. Chem. Soc.* **143**, 12524–12534 (2021).
51. Nørskov, J. K. et al. Origin of the overpotential for oxygen reduction at a fuel-cell cathode. *J. Phys. Chem. B* **108**, 17886–17892 (2004).
52. Svane, K. L. & Rossmeisl, J. Theoretical optimization of compositions of high-entropy oxides for the oxygen evolution reaction. *Angew. Chem. Int. Ed.* **61**, e202201146 (2022).
53. Hubert, M. A. et al. Acidic oxygen evolution reaction activity–stability relationships in Ru-based pyrochlores. *ACS Catal.* **10**, 12182–12196 (2020).
54. Peng, H.-J., Tang, M. T., Halldin Stenlid, J., Liu, X. & Abild-Pedersen, F. Trends in oxygenate/hydrocarbon selectivity for electrochemical $CO_{(2)}$ reduction to C_2 products. *Nat. Commun.* **13**, 1399 (2022).
55. Hu, B., Kuo, D.-Y., Paik, H., Schlom, D. G. & Suntivich, J. Enthalpy and entropy of oxygen electroadsorption on $RuO_2(110)$ in alkaline media. *J. Chem. Phys.* **152**, 094704 (2020).
56. Gottesfeld, S., McIntyre, J., Beni, G. & Shay, J. Electrochromism in anodic iridium oxide films. *Appl. Phys. Lett.* **33**, 208–210 (1978).
57. Ping, Y., Nielsen, R. J. & Goddard, W. A. III The reaction mechanism with free energy barriers at constant potentials for the oxygen evolution reaction at the $IrO_2(110)$ surface. *J. Am. Chem. Soc.* **139**, 149–155 (2017).
58. Dickens, C. F., Kirk, C. & Nørskov, J. K. Insights into the electrochemical oxygen evolution reaction with ab initio calculations and microkinetic modeling: beyond the limiting potential volcano. *J. Phys. Chem. C* **123**, 18960–18977 (2019).
59. Trimarco, D. B. et al. Enabling real-time detection of electrochemical desorption phenomena with sub-monolayer sensitivity. *Electrochim. Acta* **268**, 520–530 (2018).
60. Scott, S. B. et al. The low overpotential regime of acidic water oxidation part I: the importance of O_2 detection. *Energy Environ. Sci.* **15**, 1977–1987 (2022).
61. Zheng, Y.-R. et al. Monitoring oxygen production on mass-selected iridium–tantalum oxide electrocatalysts. *Nat. Energy* **7**, 55–64 (2022).
62. Kluge, R. M., Haid, R. W. & Bandarenka, A. S. Assessment of active areas for the oxygen evolution reaction on an amorphous iridium oxide surface. *J. Catal.* **396**, 14–22 (2021).
63. Klingan, K. et al. Water oxidation by amorphous cobalt-based oxides: volume activity and proton transfer to electrolyte bases. *ChemSusChem* **7**, 1301–1310 (2014).
64. González-Flores, D. et al. Heterogeneous water oxidation: surface activity versus amorphization activation in cobalt phosphate catalysts. *Angew. Chem. Int. Ed.* **54**, 2472–2476 (2015).
65. Pasquini, C. et al. H/D isotope effects reveal factors controlling catalytic activity in Co-based oxides for water oxidation. *J. Am. Chem. Soc.* **141**, 2938–2948 (2019).
66. Bitter, R., Mohiuddin, T. & Nawrocki, M. *LabVIEW: Advanced Programming Techniques* (CRC Press, 2017).
67. Enkovaara, J. et al. Electronic structure calculations with GPAW: a real-space implementation of the projector augmented-wave method. *J. Phys. Condens. Matter* **22**, 253202 (2010).
68. Mortensen, J. J., Hansen, L. B. & Jacobsen, K. W. Real-space grid implementation of the projector augmented wave method. *Phys. Rev. B* **71**, 035109 (2005).
69. Larsen, A. H. et al. The atomic simulation environment—a Python library for working with atoms. *J. Phys. Condens. Matter* **29**, 273002 (2017).
70. Hammer, B., Hansen, L. B. & Nørskov, J. K. Improved adsorption energetics within density-functional theory using revised Perdew–Burke–Ernzerhof functionals. *Phys. Rev. B* **59**, 7413–7421 (1999).
71. Rogers, D. B., Shannon, R. D., Sleight, A. W. & Gillson, J. L. Crystal chemistry of metal dioxides with rutile-related structures. *Inorg. Chem.* **8**, 841–849 (1969).
72. Bestaoui, N., Deniard, P. & Brec, R. Structural study of a hollandite-type K_xIrO_2 . *J. Solid State Chem.* **118**, 372–377 (1995).

Acknowledgements

I.E.L.S., J.R.D., R.R.R. and C.L. would like to acknowledge the funding and technical support from BP through the BP International Centre for Advanced Materials (bp-ICAM) as well as the EPSRC grant EP/W033232/1 which made this research possible. C.L. acknowledges the Imperial College London and China Scholarship Council for the IC–CSC joint scholarship. K.L.S., A.M.F. and J.R. acknowledge the Danish National Research Foundation Center for High-Entropy Alloy Catalysis (CHEAC) DNRF-149. We acknowledge Diamond Light Source for time on Beamline B18 under Proposal SP30396. This work was supported by EPSRC grant EP/W033232/. S.B.S. acknowledges an Energy for Future fellowship from the Iberdrola Foundation. I.E.L.S. and S.B.S. acknowledge funding from ERC grant under the European Union’s Horizon 2020 research and innovation program (Grant no. 866402).

Author contributions

C.L., R.R.R., I.E.L.S. and J.R.D. conceived the idea. C.L., R.R.R. and B.M. performed the XAS experiments. C.L. performed the optical spectroscopy measurements; B.M. custom-built the optical spectroscopy set-up. The code for linear combination fitting of the optical spectroscopy data was developed by M.S. and adapted by C.L., who analysed the data with the help of R.R.R., J.R.D., I.E.L.S., S.B.S., B.M. and J.M. The DFT calculations were performed by K.L.S., A.M.F. and J.R., who also analysed the results. J.H.L.H. performed the ToF-SIMS experiments; M.P.R. and D.J.R. supervised the experiments and contributed to the data analysis. The manuscript was written by C.L.; all authors reviewed and edited the manuscript.

Competing interests

The authors declare no competing interests.

Additional information

Supplementary information The online version contains supplementary material available at <https://doi.org/10.1038/s41929-024-01168-7>.

Correspondence and requests for materials should be addressed to Reshma R. Rao, Jan Rossmeisl, James R. Durrant or Ifan E. L. Stephens.

Peer review information *Nature Catalysis* thanks Holger Dau, Rik V. Mom and the other, anonymous, reviewer(s) for their contribution to the peer review of this work.

Reprints and permissions information is available at www.nature.com/reprints.

Publisher's note Springer Nature remains neutral with regard to jurisdictional claims in published maps and institutional affiliations.

Open Access This article is licensed under a Creative Commons Attribution 4.0 International License, which permits use, sharing,

adaptation, distribution and reproduction in any medium or format, as long as you give appropriate credit to the original author(s) and the source, provide a link to the Creative Commons licence, and indicate if changes were made. The images or other third party material in this article are included in the article's Creative Commons licence, unless indicated otherwise in a credit line to the material. If material is not included in the article's Creative Commons licence and your intended use is not permitted by statutory regulation or exceeds the permitted use, you will need to obtain permission directly from the copyright holder. To view a copy of this licence, visit <http://creativecommons.org/licenses/by/4.0/>.

© The Author(s) 2024